

1

2 **The ANTsX Ecosystem for Precision
3 Spatiotemporal Mapping of the Mouse Brain**

4 Nicholas J. Tustison¹, Min Chen², Fae N. Kronman³, Jeffrey T. Duda², Clare Gamlin⁴,
5 Lydia Ng⁴, Yongsoo Kim³, and James C. Gee²

6 ¹Department of Radiology and Medical Imaging, University of Virginia, Charlottesville, VA

7 ²Department of Radiology, University of Pennsylvania, Philadelphia, PA

8 ³Department of Neural and Behavioral Sciences, Penn State University, Hershey, PA

9 ⁴Allen Institute for Brain Science, Seattle, WA

10

11 Corresponding author:

12 Nicholas J. Tustison, DSc

13 Department of Radiology and Medical Imaging

14 University of Virginia

15 ntustison@virginia.edu

¹⁶ **Abstract**

¹⁷ Precision mapping techniques coupled with high resolution image acquisition of the mouse
¹⁸ brain permit the study of the spatial organization of gene activity and their mutual interac-
¹⁹ tion for a comprehensive view of salient structural/functional relationships. Such research
²⁰ is facilitated by standardized anatomical coordinate systems, such as the well-known Allen
²¹ Common Coordinate Framework version 3 (CCFv3), and the ability to map to such refer-
²² ence atlases. The Advanced Normalization Tools Ecosystem (ANTsX) is a comprehensive
²³ open-source software image analysis toolkit with applicability to multiple organ systems,
²⁴ modalities, and animal species. Herein, we illustrate the utility of ANTsX for generating
²⁵ precision spatial mappings of the mouse brain of different developmental ages including the
²⁶ prerequisite preprocessing steps. Additionally, as a further illustration of ANTsX capabil-
²⁷ ities, we use these publicly available mouse brain atlases to generate a velocity flow-based
²⁸ mapping encompassing the entire developmental trajectory, which we also make available to
²⁹ the public.

30 Over the past two decades there has been a notable increase in significant advancements in
31 mesoscopic analysis of the mouse brain. It is now possible to track single cell neurons in 3-D
32 across full mouse brains,¹ observe whole brain developmental changes on a cellular level,²
33 associate brain regions and tissues with their genetic composition,³ and locally characterize
34 neural connectivity.⁴ Much of this scientific achievement has been made possible due to
35 breakthroughs in high resolution imaging techniques that permit submicron, 3-D imaging
36 of whole mouse brains. Associated research techniques such as micro-optical sectioning
37 tomography,⁶ tissue clearing,^{1,7} spatial transcriptomics⁹ are all well-utilized in the course of
38 scientific investigations of mesoscale relationships in the mouse brain.

39 An important component of these research programs is the ability to map the various image
40 data to anatomical reference frames¹¹ for inferring spatial relationships between structures,
41 cells, and genetics in the brain. This has motivated the development of detailed structural
42 image atlases of the mouse brain. Notable examples include the Allen Brain Atlas and
43 Coordinate Frameworks¹³ and the Waxholm Space.¹⁴ Despite the significances of these con-
44 tributions, challenges still exist in large part due to the wide heterogeneity in associated
45 study-specific image data. Variance in the acquisition methods can introduce artifacts such
46 as tissue distortion, holes, bubbles, folding, tears, and missing slices. These severely compli-
47 cate assumptions of mapping correspondence for conventional registration approaches.

48 To address such challenges, several software packages have been developed over the years
49 comprising solutions of varying comprehensibility, sophistication, and availability. An early
50 contribution to the community was the Rapid Automatic Tissue Segmentation (RATS)
51 package¹⁵ for brain extraction (available upon request). Of the publicly available pack-
52 ages, most, if not all rely on well-established package dependencies originally developed on
53 human brain data. Another early tool was SPMMouse¹⁶ based on the well-known Statistical
54 Parametric Mapping (SPM) software package.¹⁷ The automated mouse atlas propagation
55 (aMAP) tool is largely a front-end for the NiftyReg image registration package¹⁸ applied
56 to mouse data which is currently available as a Python module.¹⁹ NiftyReg is also used by
57 the Atlas-based Imaging Data Analysis (AIDA) MRI pipeline²⁰ as well as the Multi Atlas
58 Segmentation and Morphometric Analysis Toolkit (MASMAT). Whereas the former also in-

59 corporates the FMRIB Software Library (FSL)²¹ for brain extraction and DSISTudio²² for
60 DTI processing, the latter uses NiftySeg and multi-consensus labeling tools²³ for brain extrac-
61 tion and parcellation. In addition, MASMAT incorporates N4 bias field correction²⁴ from the
62 Advanced Normalization Tools Ecosystem (ANTsX)²⁵ as do the packages Multi-modal Image
63 Registration And Connectivity anaLysis (MIRACL),²⁶ Saamba-MRI,²⁷ and Small Animal
64 Magnetic Resonance Imaging (SAMRI).²⁸ However, whereas Saamba-MRI uses AFNI²⁹ for
65 image registration; MIRACL, SAMRI, and BrainsMap³⁰ all use ANTsX tools for comput-
66 ing image-based correspondences. Other packages use landmark-based approaches to image
67 registration including SMART—³¹an R package for semi-automated landmark-based regis-
68 tration and segmentation of mouse brain based on WholeBrain.³² FriendlyClearMap³³ uses
69 the landmark-based registration functionality of Elastix.³⁴ Finally, the widespread adoption
70 of deep learning techniques has also influenced development in mouse brain imaging method-
71 ologies. For example, if tissue deformations are not a problematic artifact, DeepSlice can
72 be used to determine affine mappings³⁵ with the computational efficiency associated with
73 neural networks.

74 As noted above, many of the existing approaches for image data processing of mouse brain
75 use ANTsX tools for core steps in various workflows, particularly its pairwise, intensity-
76 based image registration tools and bias field correction. Historically, ANTsX development
77 is originally based on fundamental approaches to image mapping^{36–38} which resulted in such
78 core contributions to the field as the Symmetric Normalization (SyN) algorithm.³⁹ Since
79 its development, various independent platforms have been used to evaluate ANTsX image
80 registration capabilities in the context of different application foci (e.g., multi-site brain
81 MRI data,⁴⁰ pulmonary CT data),⁴¹ and most recently multi-modal brain registration in the
82 presence of tumors.⁴²

83 Apart from its founding contribution, ANTsX is a comprehensive biological and medical
84 image analysis toolkit, that comprises additional functionality such as template generation,
85 general data approximation, and deep learning networks specifically trained for mouse data
86 (see Table 1). The collective use of the toolkit has demonstrated superb performance in
87 multiple application areas (e.g., consensus labeling,⁴³ brain tumor segmentation,⁴⁴ and car-

Table 1: Sampling of ANTsX functionality

<i>ANTsPy: Preprocessing</i>	
bias field correction	<code>n4_bias_field_correction(...)</code>
image denoising	<code>denoise_image(...)</code>
<i>ANTsPy: Registration</i>	
image registration	<code>registration(...)</code>
template generation	<code>build_template(...)</code>
landmark registration	<code>fit_transform_to_paired_points(...)</code>
time-varying landmark reg.	<code>fit_time_varying_transform_to_point_sets(...)</code>
integrate velocity field	<code>integrate_velocity_field(...)</code>
invert displacement field	<code>invert_displacement_field(...)</code>
<i>ANTsPy: Segmentation</i>	
MRF-based registration	<code>atropos(...)</code>
Joint label fusion	<code>joint_label_fusion(...)</code>
diffeomorphic thickness	<code>kelly_kapowski(...)</code>
<i>ANTsPy: Miscellaneous</i>	
Regional intensity statistics	<code>label_stats(...)</code>
Regional shape measures	<code>label_geometry_measures(...)</code>
B-spline approximation	<code>fit_bspline_object_to_scattered_data(...)</code>
Visualize images and overlays	<code>plot(...)</code>
<i>ANTsPyNet</i>	
brain extraction	<code>mouse_brain_extraction(...modality="t2"...)</code> <code>mouse_brain_extraction(...modality="ex5"...)</code>
foreground extraction	<code>mouse_histology_brain_mask(...)</code>
midline segmentation	<code>mouse_histology_hemispherical_coronal_mask(...)</code>
cerebellum segmentation	<code>mouse_histology_cerebellum_mask(...)</code>
super resolution	<code>mouse_histology_super_resolution(...)</code>

ANTsX provides state-of-the-art open-science functionality for processing image data. Such tools, including deep learning networks, support a variety of mapping-related tasks. A more comprehensive listing of ANTsX tools with self-contained R and Python examples is provided as a gist page on GitHub (<https://tinyurl.com/antsxtutorial>).

88 diac motion estimation).⁴⁵ Importantly, ANTs is built on the Insight Toolkit (ITK) deriving
 89 benefit from a very capable open-source community of scientists and programmers as well
 90 as providing a venue for algorithmic contributions.

91 Results

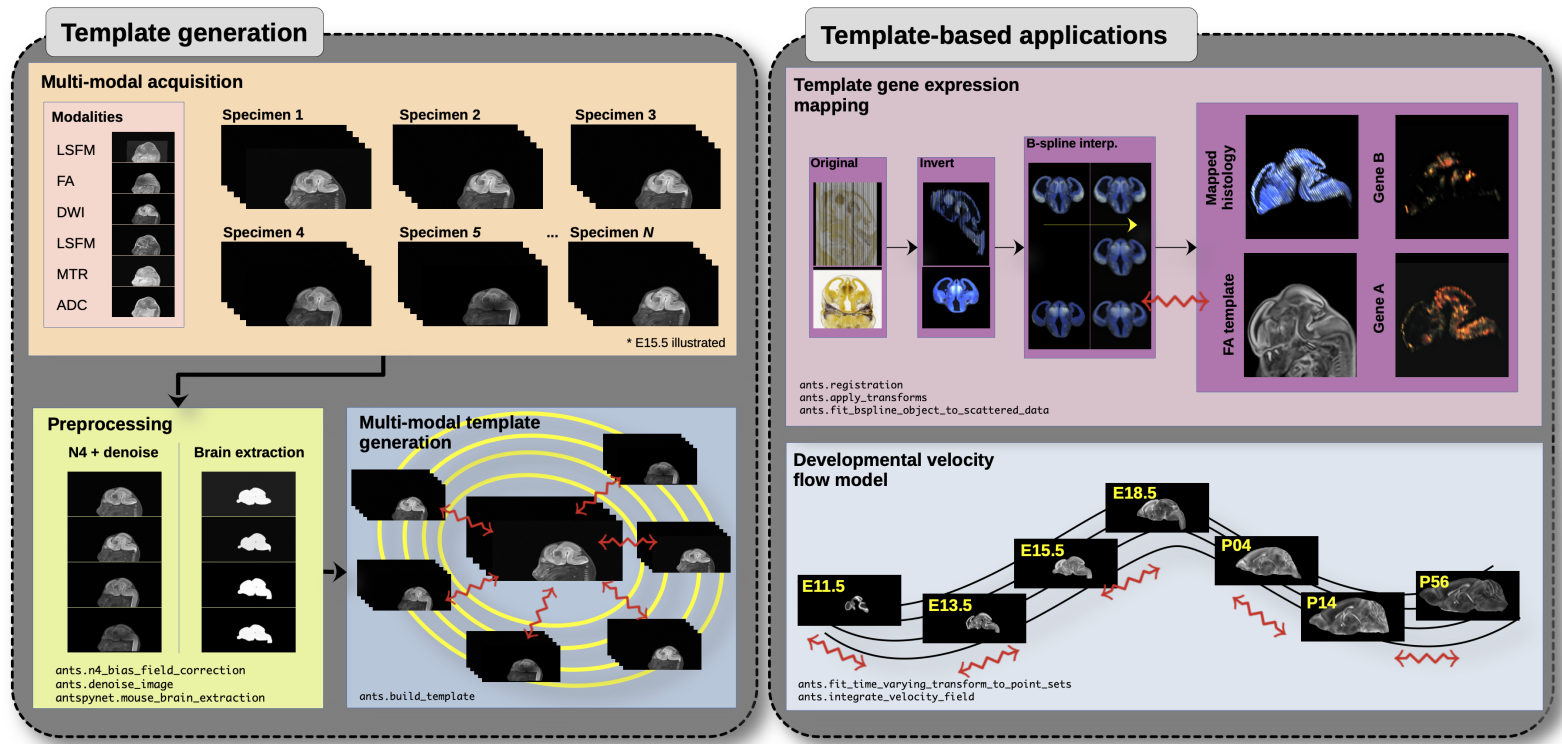


Figure 1: Illustration of a mouse brain template generation workflow and related template-based applications demonstrating the utility of different ANTsX tools. After imaging acquisition of the study population, various preprocessing steps are applied to the imaging data such as bias correction, denoising, and brain extraction as dictated by the needs of the study protocol. Not shown is the possibility of template symmetrization by contralaterally flipping the image data associated with each specimen. In the case of the DevCCF, applications include gene expression mapping and the associated velocity flow model for pseudo-template generation.

92 Recently, the developmental common coordinate framework (DevCCF) was introduced to
 93 the mouse brain research community as a public resource.⁴⁶ These symmetric atlases, com-
 94 prising both multimodal image data and anatomical segmentations defined by developmental

95 ontology, span the mouse embryonic days (E) 11.5, E13.5, E15.5, E18.5 and postnatal day
 96 (P) 4, P14, and P56 with Allen CCFv3 integration with the P56 template. Modalities include
 97 at least four MRI contrasts and light sheet fluorescence microscopy (LSFM) per develop-
 98 mental stage. Gene expression and other cell type data were mapped to the corresponding
 99 developmental time point to guide the associated anatomical parcellations. In addition to
 100 conventional preprocessing (e.g., bias field correction, brain extraction) difficulties for the
 101 various mapping tasks included tissue distortion, missing slices, and acquisition artifacts.
 102 We illustrate the utility of the ANTsX ecosystem in providing solutions for these issues in
 103 constructing the DevCCF. In addition, we also demonstrate ANTsX functionality in the
 104 generation of a single diffeomorphic transformation model⁴⁷ between developmental stages
 105 where mappings between any two continuous time points within the temporal span of the
 106 E11.5 and P56 atlases is determined by integration of the governing time-varying velocity
 107 field.⁴⁸ Such transformations permit the possibility of “pseudo” templates generated between
 108 available developmental stages, which we also demonstrate.

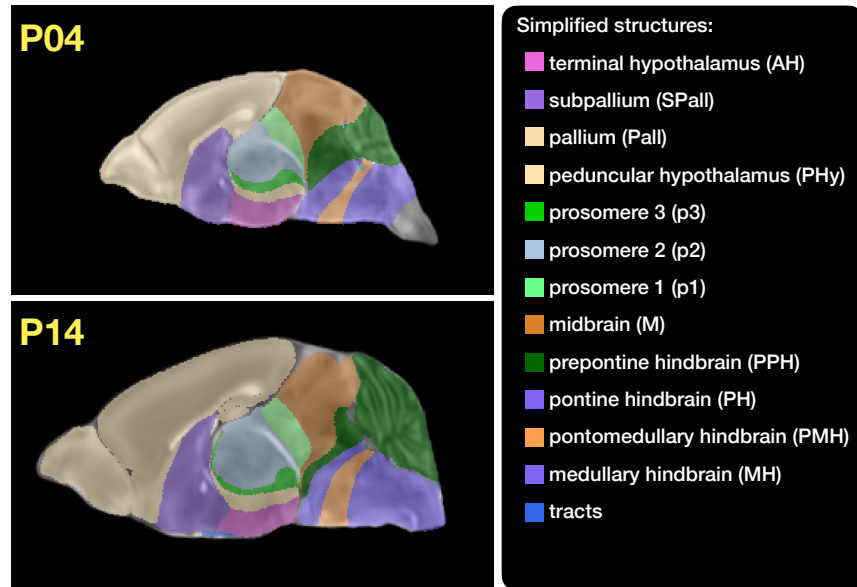


Figure 2

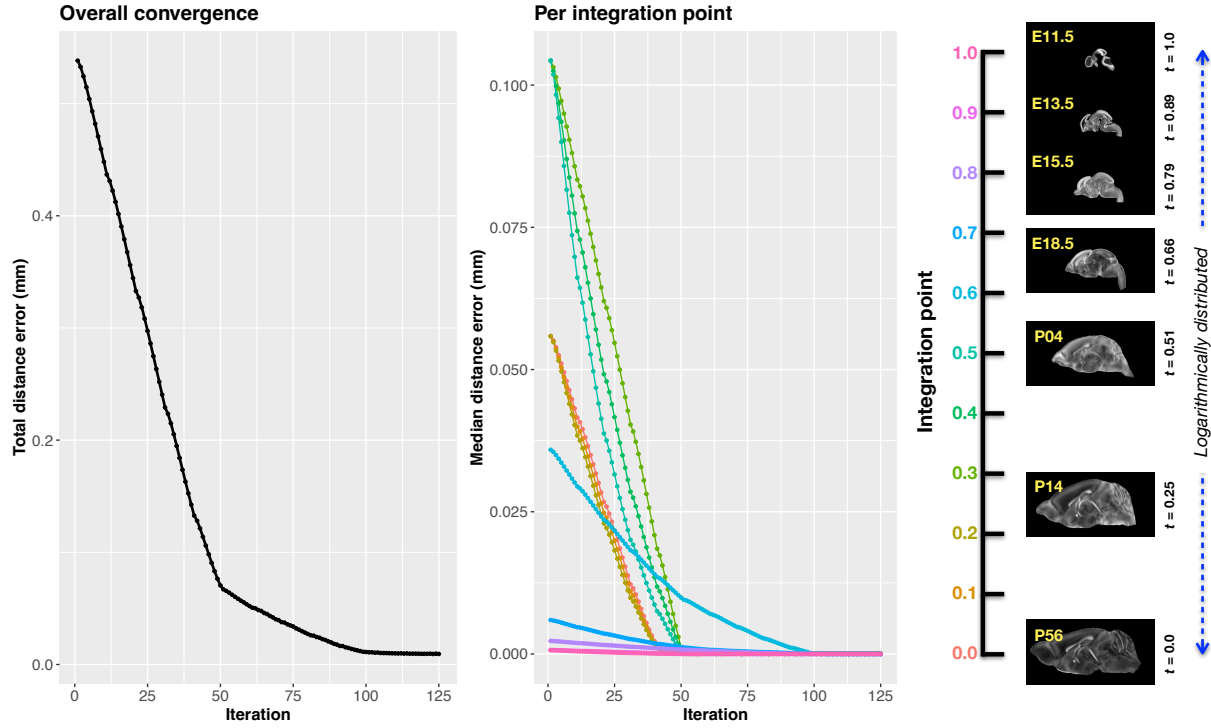


Figure 3: Convergence of the optimization of the velocity field for describing the transformation through the developmental stages from E11.5 through P56.

109 Methods

110 Preprocessing: bias field correction and denoising

111 As in human studies, bias field correction and image denoising are standard preprocessing
 112 steps in improving overall image quality in mouse brain images. The bias field, a gradual
 113 spatial intensity variation in images, can arise from various sources such as magnetic field in-
 114 homogeneity or acquisition artifacts, leading to distortions that can compromise the quality
 115 of brain images. Correcting for bias fields ensures a more uniform and consistent representa-
 116 tion of brain structures, enabling accurate quantitative analysis. Additionally, brain images
 117 are often susceptible to various forms of noise, which can obscure subtle features and affect
 118 the precision of measurements. Denoising techniques help mitigate the impact of noise, en-
 119 hancing the signal-to-noise ratio and improving the overall image quality. The well-known
 120 N4 bias field correction algorithm²⁴ has its origins in the ANTs toolkit which was imple-
 121 mented and introduced into the ITK toolkit. Similarly, ANTsX contains an implementation

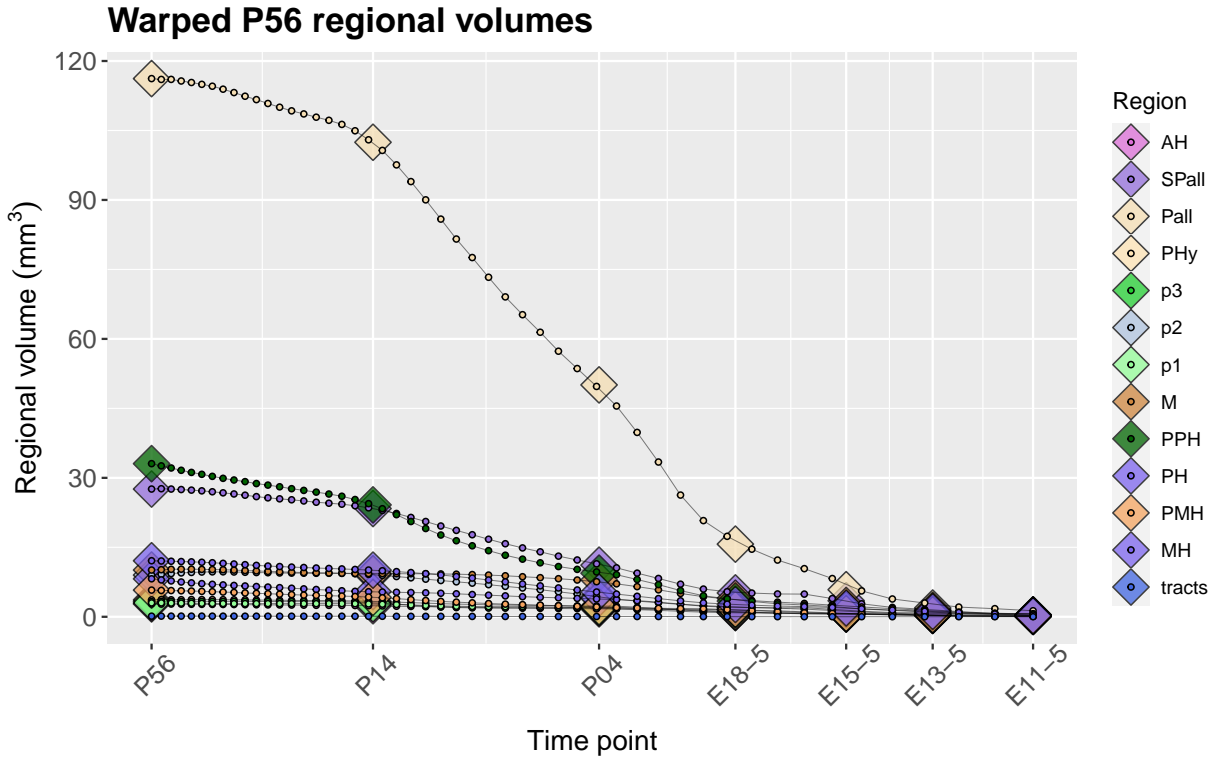


Figure 4: Warped P56.

¹²² of a well-performing patch-based denoising technique⁴⁹ and is also available as a image filter
¹²³ to the ITK community.

¹²⁴ ANTsXNet mouse brain applications

¹²⁵ *General notes regarding deep learning training.*

¹²⁶ All network-based approaches described below were implemented and organized in the
¹²⁷ ANTsXNet libraries comprising Python (ANTsPyNet) and R (ANTsRNet) analogs using the
¹²⁸ Keras/Tensorflow libraries available as open-source in ANTsX GitHub repositories. For the
¹²⁹ various applications, both share the identically trained weights for mutual reproducibility.
¹³⁰ Training data was provided by manual labeling by various co-authors and expanded using
¹³¹ both intensity-based and shape-based data augmentation techniques.

¹³² Intensity-based data augmentation consisted of randomly added noise based on ITK
¹³³ functionality, simulated bias fields based on N4 bias field modeling, and histogram

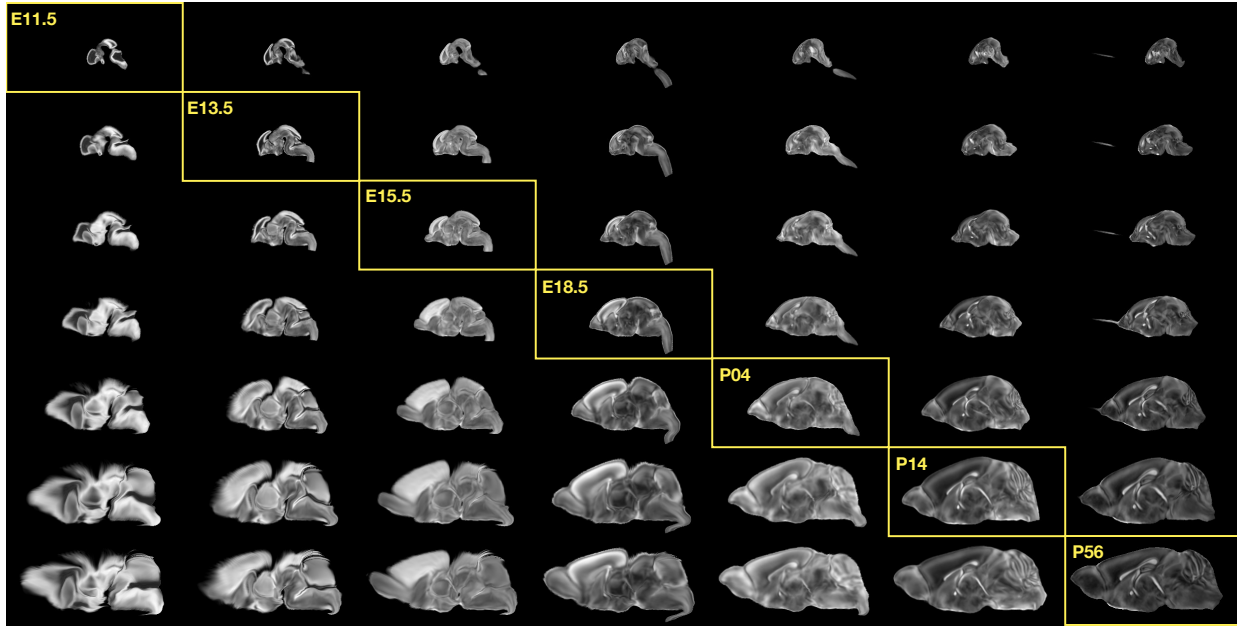


Figure 5: Mid-sagittal visualization of the effects of the transformation model in warping every developmental stage to the time point of every other developmental stage. The original images are located along the diagonal. Columns correspond to the warped original image whereas the rows represent the reference space to which each image is warped.

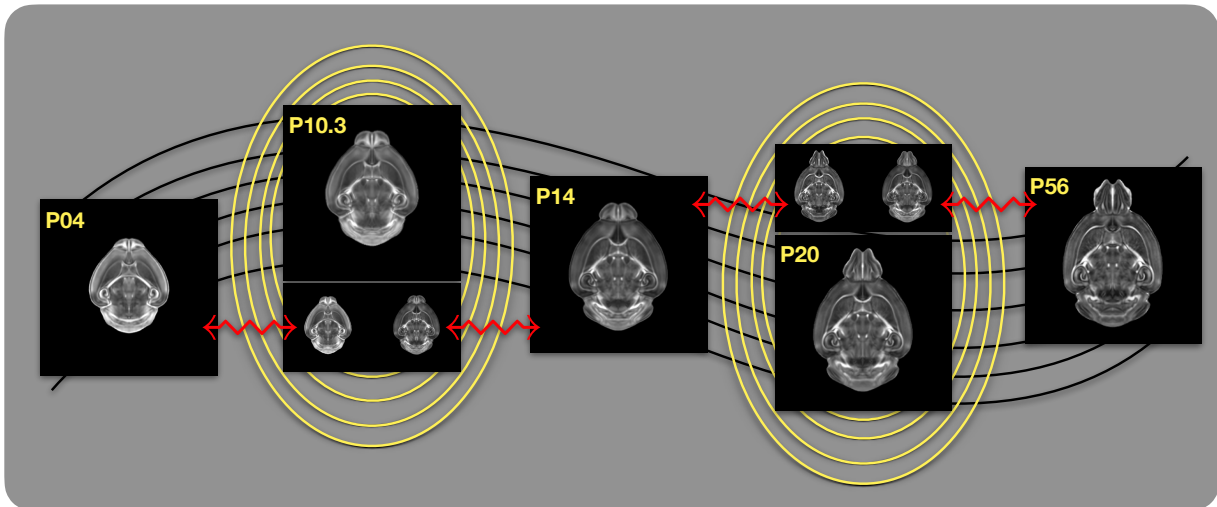


Figure 6: Illustration of the use of the velocity flow model for creating pseudo-templates at continuous time points not represented in one of the existing developmental stages. For example, FA templates at time point P10.3 and P20 can be generated by warping the existing temporally adjacent developmental templates to the target time point and using those images in the ANTsX template building process.

¹³⁴ warping for mimicking well-known MRI intensity nonlinearities.^{25,50} These augmentation
¹³⁵ techniques are available in ANTsXNet (only ANTsPyNet versions are listed): simulated
¹³⁶ bias field: `simulate_bias_field(...)`, image noise: `add_noise_to_image(...)`, and
¹³⁷ MRI intensity nonlinear characterization: `histogram_warp_image_intensities(...)`.
¹³⁸ Shape-based data augmentation used both random linear and nonlinear deformations. This
¹³⁹ functionality is also instantiated within ANTsXNet in terms of random spatial warping:
¹⁴⁰ `randomly_transform_image_data(...)`.

¹⁴¹ For all GPU training, we used Python scripts for creating custom batch generators. As such
¹⁴² batch generators tend to be application-specific, we store them in a separate GitHub reposi-
¹⁴³ tory for public availability (<https://github.com/ntustison/ANTsXNetTraining>). In terms of
¹⁴⁴ GPU hardware, all training was done on a DGX (GPUs: 4X Tesla V100, system memory:
¹⁴⁵ 256 GB LRDIMM DDR4).

¹⁴⁶ *Brain extraction.*

¹⁴⁷ Similar to human neuroimage processing, brain extraction is a crucial preprocessing step for
¹⁴⁸ accurate brain mapping. Within ANTsXNet, we have created several deep learning networks
¹⁴⁹ for brain extraction for several image modalities (e.g., T1, FLAIR, fractional anisotropy).
¹⁵⁰ Similarly, for the developmental brain atlas work⁴⁶ we developed similar functionality for
¹⁵¹ mouse brains of different modalities and developmental age. All networks use a conventional
¹⁵² 2-D U-net architecture⁵¹ and perform prediction in a slice-wise fashion given the limitations of
¹⁵³ the acquisition protocols (e.g., missing slices, slice thickness). Currently, coronal and sagittal
¹⁵⁴ networks are available for both E13.5 and E15.5 data and coronal network for T2-weighted
¹⁵⁵ MRI. In ANTsPyNet, this functionality is available in the program `brain_extraction(...)`.
¹⁵⁶ Even when physical brain extraction is performed prior to image acquisition, artifacts, such
¹⁵⁷ as bubbles or debris, can complicate subsequent processing. Similar to the brain extraction
¹⁵⁸ networks, a 2-D U-net architecture⁵¹ was created to separate the background and foreground.

¹⁵⁹ *Miscellaneous networks: Super-resolution, cerebellum, and hemispherical masking.*

¹⁶⁰ To further enhance the data prior to designing mapping protocols, additional networks were
¹⁶¹ created. A well-performing deep back projection network⁵² was ported to ANTsXNet and
¹⁶² expanded to 3-D for various super-resolution applications,⁵³ including mouse data. Finally,

₁₆₃ features of anatomical significance, namely the cerebellum and hemispherical midline were
₁₆₄ captured in these data using deep learning networks.

₁₆₅ **Image registration**

₁₆₆ **Intra-slice image registration with missing slice imputation**

₁₆₇ Volumetric gene expression slice data was collated into 3-D volumes using ... (ask Jeff).
₁₆₈ Prior to mapping this volume to the corresponding structural data and, potentially, to the
₁₆₉ appropriate template, alignment was improved using deformable registration on contiguous
₁₇₀ slices. However, one of the complications associated with these image data was the un-
₁₇₁ known number of missing slices, the number of consecutive missing slices, and the different
₁₇₂ locations of these missing slices. To handle this missing data problem, we found that data
₁₇₃ interpolation using the B-spline approximation algorithm cited earlier⁵⁴ (ANTsPy function:
₁₇₄ `fit_bspline_object_to_scattered_data(...)`). This provided sufficient data interpo-
₁₇₅ lation fidelity to perform continuous slicewise registration. Other possible variants that
₁₇₆ were considered but deemed unnecessary was performing more than one iteration cycling
₁₇₇ through data interpolation and slicewise alignment. The other possibility was incorporating
₁₇₈ the super-resolution technique described earlier. But again, our data did not require these
₁₇₉ additional steps.

₁₈₀ **Template generation**

₁₈₁ ANTsX provides functionality for constructing templates from a set (or multi-modal sets) of
₁₈₂ input images as originally described⁵⁵ and recently used to create the DevCCF templates.⁴⁶
₁₈₃ An initial template estimate is constructed from an existing subject image or a voxelwise
₁₈₄ average derived from a rigid pre-alignment of the image population. Pairwise registration
₁₈₅ between each subject and the current template estimate is performed using the Symmetric
₁₈₆ Normalization (SyN) algorithm.³⁹ The template estimate is updated by warping all subjects
₁₈₇ to the space of the template, performing a voxelwise average, and then performing a “shape

¹⁸⁸ update” of this latter image by warping it by the average inverse deformation, thus yielding
¹⁸⁹ a mean image of the population in terms of both the intensity and shape.

¹⁹⁰ Continuous developmental velocity flow transformation model

¹⁹¹ Given multiple, linearly or non-linearly ordered point sets where individual points across
¹⁹² are in one-to-one correspondence, we developed an approach for generating a velocity flow
¹⁹³ transformation model to describe a time-varying diffeomorphic mapping as a variant of the
¹⁹⁴ inexact landmark matching solution of Joshi and Miller.⁴⁷ Integration of the resulting velocity
¹⁹⁵ field can then be used to describe the displacement between any two time points within this
¹⁹⁶ time-parameterized domain. Regularization of the sparse correspondence between point sets
¹⁹⁷ is performed using a generalized B-spline scattered data approximation technique,⁵⁴ also
¹⁹⁸ developed by the ANTsX developers and contributed to ITK.

¹⁹⁹ To apply this methodology to the developmental templates,⁴⁶ we coalesced the manual par-
²⁰⁰ cellations of the developmental templates into 26 common anatomical regions (13 per hemi-
²⁰¹ sphere). We then used these regions to generate invertible transformations between suc-
²⁰² cessive time points. Specifically each label was used to create a pair of single region images
²⁰³ resulting in 26 pairs of “source” and “target” images. The multiple image pairs were used
²⁰⁴ to iteratively estimate a diffeomorphic pairwise transform. Given the seven atlases E11.5,
²⁰⁵ E13.5, E15.5, E18.5, P4, P14, and P56, this resulted in 6 sets of transforms between suc-
²⁰⁶ cessive time points. Given the relative sizes between atlases, on the order of 10^6 points were
²⁰⁷ randomly sampled labelwise in the P56 template space and propagated to each successive
²⁰⁸ atlas providing the point sets for constructing the velocity flow model. Approximately 200
²⁰⁹ iterations resulted in a steady convergence based on the average Euclidean norm between
²¹⁰ transformed point sets. Ten integration points were used and point sets were distributed
²¹¹ along the temporal dimension using a log transform for a more evenly spaced sampling.
²¹² Further details including links to data and scripts to reproduce our reported results is found
²¹³ in the associated GitHub repository.¹

²¹⁴ One potential application is the possible construction of “pseudo”-templates at currently

¹<https://github.com/ntustison/MouseBrainVelocityFlow/>

215 non-existing developmental stages.

216 **Visualization**

217 To complement the well-known visualization capabilities of R and Python, e.g., `ggplot2`
218 and `matplotlib`, respectively, image-specific visualization capabilities are available in the
219 `ants.plot(...)` (Python) and `plot.antsImage(...)` (R). These are capable of illustrating
220 multiple slices in different orientations with both other image overlays as well as label images.

₂₂₁ **References**

- ₂₂₂ 1. Keller, P. J. & Ahrens, M. B. Visualizing whole-brain activity and development at
₂₂₃ the single-cell level using light-sheet microscopy. *Neuron* **85**, 462–83 (2015).
- ₂₂₄ 2. La Manno, G. *et al.* Molecular architecture of the developing mouse brain. *Nature*
₂₂₅ **596**, 92–96 (2021).
- ₂₂₆ 3. Wen, L. *et al.* Single-cell technologies: From research to application. *Innovation*
₂₂₇ (*Camb*) **3**, 100342 (2022).
- ₂₂₈ 4. Oh, S. W. *et al.* A mesoscale connectome of the mouse brain. *Nature* **508**, 207–14
₂₂₉ (2014).
- ₂₃₀ 5. Gong, H. *et al.* Continuously tracing brain-wide long-distance axonal projections in
₂₃₁ mice at a one-micron voxel resolution. *Neuroimage* **74**, 87–98 (2013).
- ₂₃₂ 6. Li, A. *et al.* Micro-optical sectioning tomography to obtain a high-resolution atlas of
₂₃₃ the mouse brain. *Science* **330**, 1404–8 (2010).
- ₂₃₄ 7. Ueda, H. R. *et al.* Tissue clearing and its applications in neuroscience. *Nat Rev*
₂₃₅ *Neurosci* **21**, 61–79 (2020).
- ₂₃₆ 8. Ståhl, P. L. *et al.* Visualization and analysis of gene expression in tissue sections by
₂₃₇ spatial transcriptomics. *Science* **353**, 78–82 (2016).
- ₂₃₈ 9. Burgess, D. J. Spatial transcriptomics coming of age. *Nat Rev Genet* **20**, 317 (2019).
₂₃₉
- ₂₄₀ 10. MacKenzie-Graham, A. *et al.* A multimodal, multidimensional atlas of the C57BL/6J
₂₄₁ mouse brain. *J Anat* **204**, 93–102 (2004).
- ₂₄₂ 11. Mackenzie-Graham, A. J. *et al.* Multimodal, multidimensional models of mouse brain.
₂₄₃ *Epilepsia* **48 Suppl 4**, 75–81 (2007).
- ₂₄₄ 12. Dong, H. W. *Allen reference atlas. A digital color brain atlas of the C57BL/6J male*
₂₄₅ *mouse.* (John Wiley; Sons, 2008).

- 246 13. Wang, Q. *et al.* The allen mouse brain common coordinate framework: A 3D reference
247 atlas. *Cell* **181**, 936–953.e20 (2020).
- 248 14. Johnson, G. A. *et al.* Waxholm space: An image-based reference for coordinating
249 mouse brain research. *Neuroimage* **53**, 365–72 (2010).
- 250 15. Oguz, I., Zhang, H., Rumple, A. & Sonka, M. RATS: Rapid automatic tissue segmen-
251 tation in rodent brain MRI. *J Neurosci Methods* **221**, 175–82 (2014).
- 252 16. Sawiak, S. J., Picq, J.-L. & Dhenain, M. Voxel-based morphometry analyses of in
253 vivo MRI in the aging mouse lemur primate. *Front Aging Neurosci* **6**, 82 (2014).
- 254 17. Ashburner, J. SPM: A history. *Neuroimage* **62**, 791–800 (2012).
- 255
- 256 18. Modat, M. *et al.* Fast free-form deformation using graphics processing units. *Comput
257 Methods Programs Biomed* **98**, 278–84 (2010).
- 258 19. Tyson, A. L. *et al.* Accurate determination of marker location within whole-brain
259 microscopy images. *Sci Rep* **12**, 867 (2022).
- 260 20. Pallast, N. *et al.* Processing pipeline for atlas-based imaging data analysis of struc-
261 tural and functional mouse brain MRI (AIDAmri). *Front Neuroinform* **13**, 42 (2019).
- 262 21. Jenkinson, M., Beckmann, C. F., Behrens, T. E. J., Woolrich, M. W. & Smith, S. M.
263 FSL. *Neuroimage* **62**, 782–90 (2012).
- 264 22. Yeh, F.-C., Wedeen, V. J. & Tseng, W.-Y. I. Generalized q-sampling imaging. *IEEE
265 Trans Med Imaging* **29**, 1626–35 (2010).
- 266 23. Jorge Cardoso, M. *et al.* STEPS: Similarity and truth estimation for propagated
267 segmentations and its application to hippocampal segmentation and brain parcelation.
Med Image Anal **17**, 671–84 (2013).
- 268 24. Tustison, N. J. *et al.* N4ITK: Improved N3 bias correction. *IEEE Trans Med Imaging*
269 **29**, 1310–20 (2010).

- 270 25. Tustison, N. J. *et al.* The ANTsX ecosystem for quantitative biological and medical
imaging. *Sci Rep* **11**, 9068 (2021).
- 271
- 272 26. Goubran, M. *et al.* Multimodal image registration and connectivity analysis for inte-
gration of connectomic data from microscopy to MRI. *Nat Commun* **10**, 5504 (2019).
- 273
- 274 27. Celestine, M., Nadkarni, N. A., Garin, C. M., Bougacha, S. & Dhenain, M. Sammba-
MRI: A library for processing SmAll-MaMmal BrAin MRI data in python. *Front
Neuroinform* **14**, 24 (2020).
- 275
- 276 28. Ioanas, H.-I., Marks, M., Zerbi, V., Yanik, M. F. & Rudin, M. An optimized regis-
tration workflow and standard geometric space for small animal brain imaging. *Neu-
roimage* **241**, 118386 (2021).
- 277
- 278 29. Cox, R. W. AFNI: What a long strange trip it's been. *Neuroimage* **62**, 743–7 (2012).
- 279
- 280 30. Ni, H. *et al.* A robust image registration interface for large volume brain atlas. *Sci
Rep* **10**, 2139 (2020).
- 281
- 282 31. Jin, M. *et al.* SMART: An open-source extension of WholeBrain for intact mouse
brain registration and segmentation. *eNeuro* **9**, (2022).
- 283
- 284 32. Fürth, D. *et al.* An interactive framework for whole-brain maps at cellular resolution.
Nat Neurosci **21**, 139–149 (2018).
- 285
- 286 33. Negwer, M. *et al.* FriendlyClearMap: An optimized toolkit for mouse brain mapping
and analysis. *Gigascience* **12**, (2022).
- 287
- 288 34. Klein, S., Staring, M., Murphy, K., Viergever, M. A. & Pluim, J. P. W. Elastix: A
toolbox for intensity-based medical image registration. *IEEE Trans Med Imaging* **29**,
196–205 (2010).
- 289
- 290 35. Carey, H. *et al.* DeepSlice: Rapid fully automatic registration of mouse brain imaging
to a volumetric atlas. *Nat Commun* **14**, 5884 (2023).
- 291

- 292 36. Bajcsy, R. & Broit, C. Matching of deformed images. in *Sixth International Conference on Pattern Recognition (ICPR'82)* 351–353 (1982).
- 293
- 294 37. Bajcsy, R. & Kovacic, S. Multiresolution elastic matching. *Computer Vision, Graphics, and Image Processing* **46**, 1–21 (1989).
- 295
- 296 38. Gee, J., Sundaram, T., Hasegawa, I., Uematsu, H. & Hatabu, H. Characterization of regional pulmonary mechanics from serial magnetic resonance imaging data. *Acad Radiol* **10**, 1147–52 (2003).
- 297
- 298 39. Avants, B. B., Epstein, C. L., Grossman, M. & Gee, J. C. Symmetric diffeomorphic image registration with cross-correlation: Evaluating automated labeling of elderly and neurodegenerative brain. *Med Image Anal* **12**, 26–41 (2008).
- 299
- 300 40. Klein, A. *et al.* Evaluation of 14 nonlinear deformation algorithms applied to human brain MRI registration. *Neuroimage* **46**, 786–802 (2009).
- 301
- 302 41. Murphy, K. *et al.* Evaluation of registration methods on thoracic CT: The EMPIRE10 challenge. *IEEE Trans Med Imaging* **30**, 1901–20 (2011).
- 303
- 304 42. Baheti, B. *et al.* The brain tumor sequence registration challenge: Establishing correspondence between pre-operative and follow-up MRI scans of diffuse glioma patients. (2021).
- 305
- 306 43. Wang, H. *et al.* Multi-atlas segmentation with joint label fusion. *IEEE Trans Pattern Anal Mach Intell* **35**, 611–23 (2013).
- 307
- 308 44. Tustison, N. J. *et al.* Optimal symmetric multimodal templates and concatenated random forests for supervised brain tumor segmentation (simplified) with ANTsR. *Neuroinformatics* (2014) doi:[10.1007/s12021-014-9245-2](https://doi.org/10.1007/s12021-014-9245-2).
- 309
- 310 45. Tustison, N. J., Yang, Y. & Salerno, M. Advanced normalization tools for cardiac motion correction. in *Statistical atlases and computational models of the heart - imaging and modelling challenges* (eds. Camara, O. et al.) vol. 8896 3–12 (Springer International Publishing, 2015).
- 311

- 312 46. Kronman, F. A. *et al.* Developmental mouse brain common coordinate framework.
313 *bioRxiv* (2023) doi:[10.1101/2023.09.14.557789](https://doi.org/10.1101/2023.09.14.557789).
- 314 47. Joshi, S. C. & Miller, M. I. Landmark matching via large deformation diffeomor-
315 phisms. *IEEE Trans Image Process* **9**, 1357–70 (2000).
- 316 48. Christensen, G. E., Rabbitt, R. D. & Miller, M. I. Deformable templates using large
317 deformation kinematics. *IEEE Trans Image Process* **5**, 1435–47 (1996).
- 318 49. Manjón, J. V., Coupé, P., Martí-Bonmatí, L., Collins, D. L. & Robles, M. Adaptive
319 non-local means denoising of MR images with spatially varying noise levels. *J Magn
Reson Imaging* **31**, 192–203 (2010).
- 320 50. Nyúl, L. G., Udupa, J. K. & Zhang, X. New variants of a method of MRI scale
321 standardization. *IEEE Trans Med Imaging* **19**, 143–50 (2000).
- 322 51. Falk, T. *et al.* U-net: Deep learning for cell counting, detection, and morphometry.
323 *Nat Methods* **16**, 67–70 (2019).
- 324 52. Haris, M., Shakhnarovich, G. & Ukita, N. Deep back-projection networks for super-
325 resolution. in *2018 IEEE/CVF Conference on Computer Vision and Pattern Recog-
nition* 1664–1673 (2018). doi:[10.1109/CVPR.2018.00179](https://doi.org/10.1109/CVPR.2018.00179).
- 326 53. avants, brian *et al.* Concurrent 3D super resolution on intensity and segmentation
327 maps improves detection of structural effects in neurodegenerative disease. *medRxiv*
(2023) doi:[10.1101/2023.02.02.23285376](https://doi.org/10.1101/2023.02.02.23285376).
- 328 54. Tustison, N. J. & Amini, A. A. Biventricular myocardial strains via nonrigid registra-
329 tion of anatomical NURBS model [corrected]. *IEEE Trans Med Imaging* **25**, 94–112
(2006).
- 330 55. Avants, B. B. *et al.* The optimal template effect in hippocampus studies of diseased
331 populations. *Neuroimage* **49**, 2457–66 (2010).